Available online at www.sciencedirect.com
SCIENCE DIRECT
Earth and Planetary Science Letters 244 (2006) 590–605
EPSL
www.elsevier.com/locate/epsl

Lithospheric and sublithospheric anisotropy beneath the Baltic shield from surface-wave array analysis

Helle A. Pedersen [a,b,c,*], Marianne Bruneton [a,d], Valérie Maupin [e]
SVEKALAPKO Seismic Tomography Working Group

[a] *Laboratoire de Géophysique Interne et Tectonophysique, Grenoble University, BP 53, F-38041 Grenoble, France*
[b] *GeoForschungsZentrum Potsdam, Germany*
[c] *University of Potsdam, Germany*
[d] *Geological Survey of Canada, 615 Booth Street, Ottawa, ON, Canada K1A 0E9*
[e] *Department of Geosciences, University of Oslo, POB 1047 Blindern, 0316 Oslo, Norway*

Received 1 September 2005; received in revised form 31 January 2006; accepted 4 February 2006
Available online 30 March 2006
Editor: R.D. van der Hilst

Abstract

We report measurements of radial and azimuthal anisotropy in the upper mantle beneath southern and central Finland, which we obtained by array analysis of fundamental-mode Rayleigh and Love waves. Azimuthally averaged phase velocities were analysed in the period range 15 to 190 s for Rayleigh waves and 15 to 100 s for Love waves. The azimuthal variation of the Rayleigh wave phase velocities was obtained in the period range 20 to 100 s. The limited depth resolution of fundamental-mode surface waves necessitated strong damping constraints in the inversion for anisotropic parameters. We investigated the effects of non-unicity on the final model by experimenting with varying model geometries. The radial anisotropy beneath Finland can be explained by a lithosphere at least 200 km thick, predominantly (>50% by volume) composed of olivine crystals having their *a*-axes randomly distributed in the horizontal plane. On the contrary, the measured lithospheric azimuthal anisotropy is small. This can be reconciled with body-wave observations made in the area that indicate a complex pattern of rapidly varying anisotropy. Below 200–250 km depth, that is below the petrologic lithosphere as revealed by xenolith analyses conducted in the area, the magnitude of the azimuthal anisotropy increases and would be compatible with a mantle containing 15–20% by volume of olivine crystals whose *a*-axes are coherently aligned in the N–NE direction. The alignment of the *a*-axes is off the direction of present-day absolute plate motion in either the no-net-rotation or hot-spot reference frame, currently N55–N60. We interpret this mismatch as evidence for a complex convective flow pattern of the mantle beneath the shield, which, by inference, is decoupled from the overlying lithosphere.

Keywords: surface-waves; anisotropy; continental lithosphere; Baltic shield

1. Introduction

Seismic anisotropy in the Earth's mantle is the signature of past or ongoing mantle deformation. Of particular interest are shields for which the composition and thickness of the lithosphere are still open to debate [1–5].

* Corresponding author. LGIT-Maison des Géosciences, BP 53, 38041 Grenoble Cedex 9, France. Tel.: +33 4 76 82 80 35; fax: +33 4 76 82 81 01.
E-mail address: Helle.Pedersen@obs.ujf-grenoble.fr (H.A. Pedersen).

0012-821X/$ - see front matter © 2006 Elsevier B.V. All rights reserved.
doi:10.1016/j.epsl.2006.02.009

Most major mantle minerals are anisotropic, but the overall anisotropy can mainly be attributed to olivine minerals. There is evidence that these minerals generally align with maximum finite strain directions associated with mantle flow [6], and some agreement exists between the predicted and the observed anisotropy for flow models [7,8]. The relationship between the mantle flow and any anisotropy is however not always simple and can be influenced by a variety of factors: deformation history [9,10], pressure and temperature [11–13], rock composition [14], water-content [15] and partial melt [16,17]. Other sources of anisotropy may be fine layering or other fine-scale structures such as fluid filled cracks [18]. For further discussion and references we refer to the reviews by Savage [19] and Silver et al. [14].

Anisotropy can be directly observed in xenoliths and ophiolite samples of the mantle lithosphere [20,21]. Indirect observations are based mainly on seismic studies of the splitting of sub-vertically propagating S-waves (SKS splitting, [19,14]) and the phase velocity of surface waves [22–27]. Such studies rarely yield similar results due to the different scales at which they operate [28].

SKS splitting analysis can detect laterally rapid (over tens of kilometers) changes in azimuth of the fast S-wave direction and in the delay between the fast and the slow directions. This kind of analysis has little depth resolution and is sensitive only to the projection of the fast axis onto the horizontal plane. The lack of depth resolution means that these data are not very suitable in determining whether the anisotropy is located in the lithosphere or in the asthenosphere, an issue that has important geodynamical implications [14,29].

Inversion of surface-wave phase velocities, on the other hand, gives information on the depth of the anisotropy. The drawback is that most surface-wave tomographic studies offer only limited lateral resolution, typically of the order of 1000–2000 km, so that comparisons with SKS measurements are difficult. To increase resolution it is necessary to use regional broadband arrays [26,30,31]. The surface-wave phase velocities can then give information on the azimuthal component of the anisotropy, which is the one identified with SKS splitting, and on the radial anisotropy part, which manifests itself through the so-called Rayleigh–Love discrepancy. The latter is sometimes so large that it cannot be explained by the alignment of anisotropic minerals [32]. It is therefore possible that the Love–Rayleigh discrepancy is only partly due to a predominantly horizontal alignment of olivine minerals.

When SKS splitting and Love–Rayleigh discrepancy are observed in the same areas, they can rarely be explained by a simple plausible model with a single anisotropic layer [33]. To better understand these differences it is necessary to study both radial and azimuthal surface-wave anisotropy at relatively small scales, e.g. by using 2D broadband networks.

Here we report on simultaneous analysis of surface-wave azimuthal and radial anisotropy beneath the SVEKALAPKO broadband array, using similar data processing methods and inversion techniques for both types of anisotropy. The use of phase-velocity measurements across the array means that the lateral resolution of the anisotropy we measure is of the order of the dimension of the array. The geographical area investigated will be the same for the two types of anisotropy. The drawback of our approach is that the available data are limited to fundamental-mode surface waves, so the depth resolution will be limited and we must impose strong smoothing in the inversions.

The SVEKALAPKO array [34] provides a unique opportunity to study the seismic anisotropy in the mantle beneath a shield. The study area is well known in terms of P-wave tomography [2], receiver functions [35] and isotropic surface-wave tomography [36,37]. The presence of xenoliths at two locations gives good constraints on lithospheric thickness [38,66] which is approximately

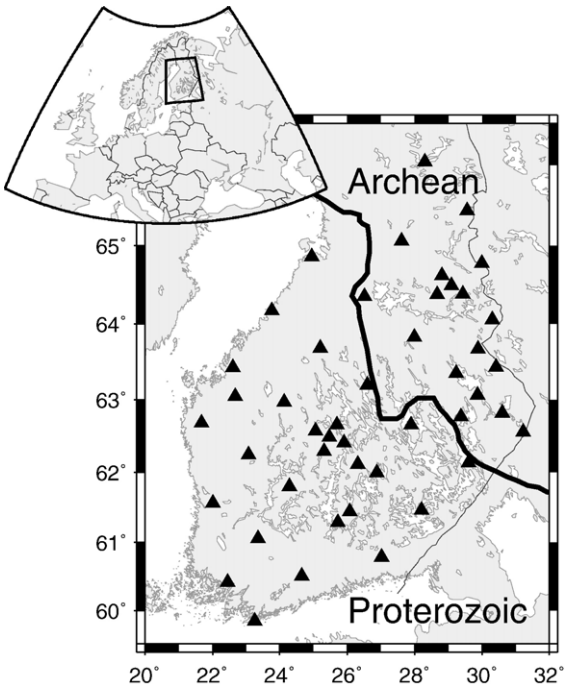

Fig. 1. Geometry of broadband stations (triangles) of the SVEKALAPKO array. The solid line shows the surface boundary between the Archean and Proterozoic domains.

225–250 km. Body-wave anisotropy studies (P residuals, SKS splitting) are currently underway ([39,40]), it should be feasible to integrate these various pieces of the puzzle into a coherent picture once the basis for each observation has been firmly established.

2. Data processing

The SVEKALAPKO array consisted of 46 broadband stations deployed on a $(500 \times 700)\,km^2$ two-dimensional grid covering the central part of the Fennoscandian Shield (Fig. 1), operational for 6 months in the winter 1998/1999. Out of the recorded teleseismic earthquakes of magnitude larger than 5.5, we preselected 69 events showing a high quality Rayleigh wave signal (see Fig. 2).

The data was first corrected for the instrument response, and we then rotated the horizontal components into radial and transverse components based on the theoretical great-circle direction. The fundamental-mode Rayleigh (Love) wave was extracted from the vertical (transverse) component of the signal using a phase-matched filter [41,42]. This part of the analysis enabled the exclusion of waves other than surface waves, and the identification and rejection of events at frequencies where we suspected interference from higher modes or strong multipathing.

The average Rayleigh and Love wave phase velocities and their azimuthal variations were calculated by a three step array analysis. The first step consisted of determining the back azimuth of the incoming surface waves. The second part consisted of determining the overall mean phase velocity, and the third part consisted of retrieving the azimuthal variation of the phase velocity. The two first parts are similar to those used by Pedersen et al. [43].

2.1. Array analysis of Rayleigh and Love dispersion for each event

This first part of the array analysis consisted of determining, for each event, the back azimuth of the incoming surface waves. For each wave (Rayleigh, Love), each event k and each station couple (i,j), the time delays $\Delta t_{ij}^{k}(f)$ were measured as a function of frequency. We used Wiener filtering [44,45] for this analysis, transforming the phase of the Wiener filter to time delays. This measurement has the advantage of objectively reducing incoherent noise, by applying a Hanning window to the auto- and cross-correlations of the two signals. The order of the Hanning window is 1 for the phase estimation and is 16 for the estimation of the coherence. At this step we rejected phases with a coherency less than 0.95 or a signal to noise ratio lower than 4 for one of the signals.

The time delays $\Delta t_{ij}^{k}(f)$ were then inverted for each event k to obtain the best slowness vector for that event, assuming that the incident wave is plane. As it is important to minimize the influence of outliers, the misfit $F_1^k(f)$ was estimated as the mean absolute difference between the observed and estimated delays. This inversion was done by searching for the back azimuth $\theta^k(f)$ for which the delay-distance points can best be described (minimal $F_1^k(f)$) by a line with slope $1/V^k(f)$ that goes through the origin. Throughout the paper we

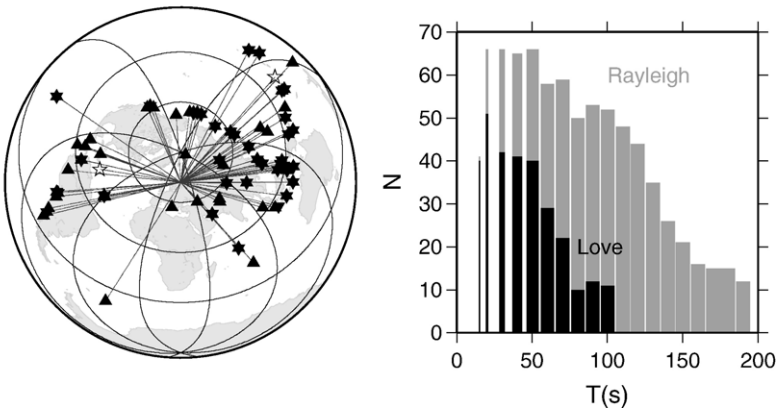

Fig. 2. Event characteristics. Left: event distribution. Upward triangles: events used for the Rayleigh waves at 50 s period; downward triangles: events used for the Love waves at 50 s period; open star: one event rejected at 50 s period but used at other periods. Right: Number of events used for the Rayleigh and Love wave dispersion measurements. The width of each column shows the width of each frequency band over which the analysis is carried out. The signal to noise ratio is generally better for Rayleigh waves as compared to Love waves, resulting in a wider period band for which dispersion measurements are possible.

use the letter V rather than C to designate phase velocities to avoid confusion with the anisotropic elastic constants. The distances $D_{ij}^k(f)$ used in this analysis are the distances between stations i and j projected onto the slowness vector. This inversion gives $\theta^k(f)$ and $V^k(f)$, the back azimuth and phase velocity associated with this best-fitting slowness vector.

2.2. Analysis of mean velocity

Using the best back azimuth for each event, we then calculated the best average velocity for the whole dataset.

$V(f)$ was determined as the inverse of the slope of the best fitting line through all $(\Delta t_{ij}^k(f), D_{ij}^k(f))$ points. We imposed that the line goes through the origin, and we used the L1 norm for the data misfit estimation. To obtain an accurate estimate we first fitted a straight line to all available $(\Delta t_{ij}^k(f), D_{ij}^k(f))$ points with an associated misfit $F_1^k(f)$ less than 4 s, as a large misfit indicates the presence of noise or diffraction, with the consequence that a plane wave is not a good solution to the delay measurements of event k at frequency f. In addition we rejected points with a misfit (in this last inversion) larger than twice the mean absolute misfit and re-estimated the phase velocity $V(f)$ and mean misfit $F_2(f)$ on the reduced dataset. Following [43] the uncertainty was estimated as $V_{\max}(f) - V(f)$ where

$$V_{\max}(f) = \frac{D_{\max}(f)}{D_{\max}(f)/V(f) - F_2(f)} \quad (1)$$

$D_{\max}(f)$ is the maximum value of $D_{ij}^k(f)$. $V_{\max}$ is the inverse of the slope of the straight line when the misfit is subtracted from the time measurement at the furthest distance. This uncertainty corresponds fairly closely to the standard deviation of all $V^k(f)$ curves in the case where the number of stations available is the same for all events [43].

Fig. 2 shows the event distribution and the final number of events used for the dispersion calculation as a function of the period. Due to a better signal to noise ratio on the vertical component, the number of events used in the Rayleigh wave analysis was significantly higher than for the Love waves. Many events are incident from back azimuths between 30° and 90°. For the Rayleigh waves the proportion of events from this azimuth range varies from 40% to 60% depending on the period. For the Love waves it varies between 50% and 100%. We discarded the periods where more than 70% of the events are incident from similar back azimuths. This means that the Rayleigh wave dispersion is measured from 15 to 190 s period and the Love wave dispersion from 15 to 100 s period. In what follows rather than using all measurements evenly spaced in frequency, we averaged the phase velocities by applying the array analysis on all the $(\Delta t_{ij}^k(f), D_{ij}^k(f))$ points within a series of narrow frequency windows (less than 0.004 Hz wide). At each target period, the window width was adjusted so that the velocities are independent from one period to the next. The window widths are shown in Fig. 2.

The average Rayleigh and Love dispersion curves are shown in Fig. 3. In this figure we include predicted Rayleigh and Love dispersion curves for an isotropic model obtained by inversion of only Rayleigh waves [36]. The mismatch between the predicted and observed Love velocities is indicative of significant radial anisotropy.

2.3. Analysis of azimuthal anisotropy

The Love wave phase velocities were not of sufficiently high quality and with sufficient azimuthal distribution for an analysis of their azimuthal variation. The Rayleigh wave phase velocities could on the other hand be analysed.

In the presence of azimuthal anisotropy, the surface-wave phase velocity dependence on the azimuth can be expressed [46] as

$$V_{\text{th}}(T) = V_{\text{aver}}(T)[1 + A\cos(2\theta) + B\sin(2\theta) + C\cos(4\theta) + D\sin(4\theta)] \quad (2)$$

$V_{\text{th}}(T)$ denotes the theoretical phase velocity of a surface wave in an azimuthally anisotropic media. $V_{\text{aver}}(T)$ is the average phase velocity and A–D are quantities

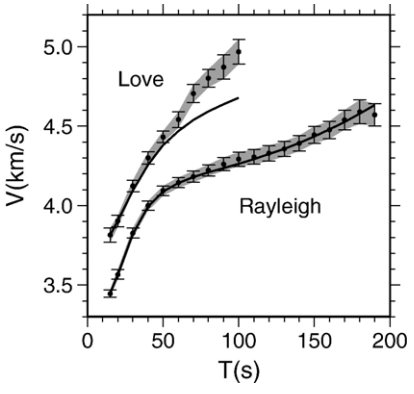

Fig. 3. Average dispersion curves for Rayleigh and Love waves (grey shading and error bars). The two solid lines correspond to the dispersion curves for a model obtained by inversion of only Rayleigh dispersion. Observed Love velocities are significantly higher than those predicted from Rayleigh waves, indicating the presence of significant radial anisotropy.

that are structure and frequency dependent. The procedures used to find the best fitting theoretical $V_{th}(T)$ showed that the 2θ terms were largely dominant, in accordance with most other studies of Rayleigh wave fundamental-mode phase velocity variations. Eq. (2) can then be rearranged into

$$V_{th}(T) = V_{aver}(T)[1 + A^*(T)\cos(2(\theta - \theta_0))] \quad (3)$$

which has more direct physical meaning as it gives the fast direction as θ_0, and the apparent percentage of anisotropy as $A^*(T)$.

We based our analysis of azimuthal anisotropy on the array analysis described in Section 2.1, which yielded for each event and frequency the back azimuth and the average phase velocity across the array. Note that the observed back azimuth may differ significantly from the great circle between the epicentre and the seismic stations [47–49]. The mean absolute deviation in our data set was 4°, while the deviations for individual events were up to 30°. In the presence of azimuthal anisotropy the $(\theta^k(f), V^k(f))$ points should follow a cosine curve as described by Eq. (3). Due to random noise and non-plane incident waves [50,51], the $(\theta^k(f), V^k(f))$ points can be expected to be strongly scattered.

Fig. 4 shows (θ_{obs}, V_{obs}) pairs for 30 and 90 s period. The colour code of the points corresponds to the misfit $F_1^k(f)$ obtained in the analysis of Section 2.1. The smaller $F_1^k(f)$, the better is the fit to a plane wave. At 30 s period the (θ_{obs}, V_{obs}) points appear randomly scattered around an average velocity of 3.83 km/s, but at 90 s period the high quality points ($F_1^k(f)$ better than 2 s) show a systematic dependency on back azimuth despite significant scatter. The question was therefore whether it was possible, in spite of the data scatter, to calculate a cosine function in the form of Eq. (3) which adequately describes the observed data and whether it was possible to provide realistic error estimates on $V_{aver}(T)$, $A^*(T)$ and θ_0.

The calculation of the best fitting cosine is in principle straightforward: using the L1 norm to minimize the influence of outliers and given a series of data points (θ_{obs}, V_{obs}), the best fitting cosine can be estimated by testing all realistic values of $V_{aver}(T)$, $A^*(T)$ and θ_0, and choosing the combination with the smallest misfit.

The practical implementation was however not so straightforward. We needed to determine the smoothing and/or weighting that should to be applied to the (θ_{obs}, V_{obs}) points, and to estimate the influence of such choices on the anisotropy estimate ($V_{aver}(T)$, $A^*(T)$ and θ_0). The estimate would obviously be meaningless if it was strongly dependent on intermediate processing choices. The analysis must also provide a meaningful error estimate on $V_{aver}(T)$, $A^*(T)$ and θ_0.

2.3.1. Procedure 1: bootstrap

We first searched for the best fitting cosine using the individual event data $(\theta^k(f), V^k(f))$ of Fig. 4. The fit to the plane wave $F_1^k(f)$ provided some insight to the quality of each data point, we therefore weighted each point by the inverse of the associated $F_1^k(f)$. To avoid dominance by a few points, we capped the weights to a maximum of 1. Even though there were events from most directions, the data were dominated by events located to the north-east of the array ($0° < \theta < 90°$), and many of them were associated with a good fit, enhancing the predominance of this direction. To downweight these events we artificially attributed a fit $F_1^k(f) = 4$ to all points corresponding to ($0° < \theta < 90°$).

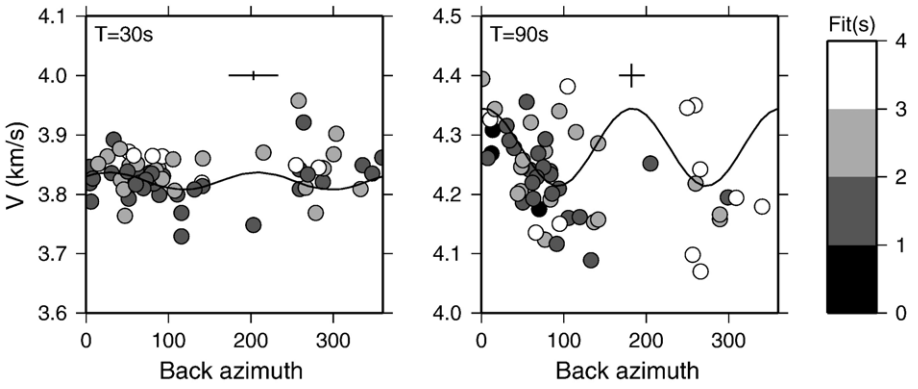

Fig. 4. Variation of Rayleigh phase velocities with azimuth for 30 s (left) and 90 s (right) period. Each point corresponds to a teleseismic event for which the phase velocity and back azimuth are obtained by array analysis. The colour code corresponds to the average L1 fit to the best straight line which defines the velocity. A perfect fit would therefore be 0. The solid black line in each figure is the best fitting cosine to the points. The uncertainties on amplitude and fast direction are indicated by the cross.

As $F_1^k(f)=4$ was also the threshold for the use of individual data points in the analysis (see Section 2.2) the ratio of maximum to minimum weight was 4.

To obtain a reliable error estimate, we chose to apply a bootstrap procedure. We created a large number of bootstrap samples of the same size as the original dataset by randomly sampling the original dataset with replacement. Each bootstrap sample had the same size of the original data set but each original data point if included could appear several times. The total number of bootstrap samples was $M=100$, and we verified that the average and the estimated errors were unchanged by using larger values of M. For each bootstrap sample m we then calculated $V_{\mathrm{aver},m}$, A^*_m and $\theta_{0,m}$. As preferred value and uncertainty for each parameter we used the average and standard deviation over all m.

The retrieved velocities V_{aver} fall within the errorbars of the dispersion curve of Bruneton et al. [36] and are undistinguishable in the smaller period range usable in this section from those obtained in Section 2.2. We therefore focus the discussion on θ_0 and A^* in this section.

Fig. 4 shows the input data and the retrieved cosines with their error bars for 30 and 90 s period. The cosines reflect quantitatively what one would expect from the event data points (θ^k, V^k) in Fig. 4: for $T=90$ s, θ_0 is constrained to be in approximately N-NNE (N350 to N20), and $A^*(T)$ is relatively well constrained. For $T=30$ s, where the data have a scatter larger than any apparent cosine function, the retrieved value of A^* is small and the uncertainty on θ_0 is large—the fast direction is between N10 and N55. We verified that the weighting applied for the cosine determination did not influence the estimated θ_0 and $A^*(T)$ beyond their associated errorbars.

2.3.2. Procedure 2: azimuth smoothing

The second approach we used was to smooth the data points prior to the estimation of the cosine parameters. To do this (for each frequency window) we regrouped the data points into back azimuth windows, and applied the array analysis of Section 2.2, but this time separately on subsets of events corresponding to back azimuths in the defined windows. We used 20° wide windows, with a 10° overlap between neighbouring windows, so every other window was independent. Note that the observed back azimuths for each event and frequency were used, rather than the event-array great circle.

Fig. 5 shows the result $(\theta_{\mathrm{smooth}}, V_{\mathrm{smooth}})$ of the smoothing for $T=30$ s and $T=90$ s. The variation with azimuth stands out more clearly than in Fig. 4, and the error bars and the number of data points are clearly correlated. The dominance of events from NE directions is strongly reduced.

We then estimated ($V_{\mathrm{aver}}(T)$, $A^*(T)$ and θ_0) by grid-search as the combination which would give the maximum misfit reduction. We subsequently maintained two of the three parameters at the best value and searched for the limits in the third one for which the misfit reduction was 90% of its maximum value. This procedure was repeated for each parameter and carried out using different weightings in the misfit calculation: a) no weighting; b) exclusion of (θ_{smooth}, V_{smooth}) points obtained with a low number of data points ($\Delta t_{ij}^k(f)$, $D_{ij}^k(f)$); c) weighting by the number of data points; d) weighting by the inverse of the uncertainty on V_{smooth}; e)

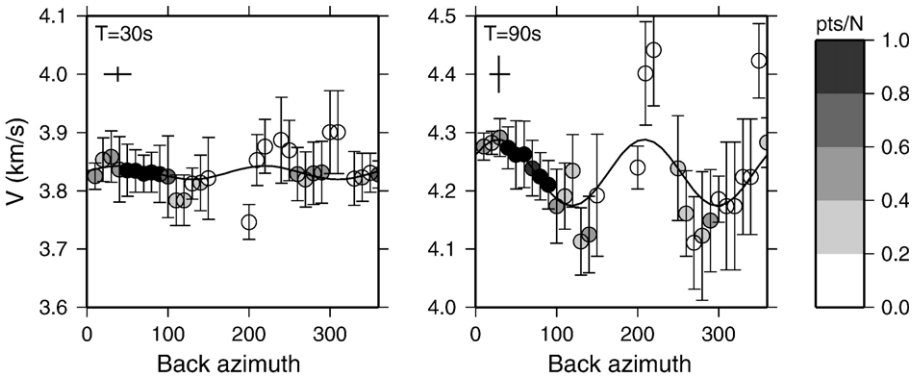

Fig. 5. Smoothed variation of Rayleigh phase velocities with azimuth for 30 s (left) and 90 s (right) period. Each point is obtained by applying array analysis on all the $(D_{ij}^k(f), \Delta t_{ij}^k(f))$ points P falling within a defined (20° wide) back azimuth window. Note that the observed back azimuths θ_k are used rather than the great-circle values. The colour scale shows $P/NN=100\,000$ at 30 s period and $N=20\,000$ at 90 s period so as to use the same colour scale. With 46 seismic stations, there are 1035 station pairs. Using a frequency and azimuth window and all station couples implies that P can be big and depends strongly on period. To obtain sufficient dynamics in the colour scale for low P, the darkest colour corresponds to $P \geq N$. The best fitting cosine (solid line) is also included in the plots. The uncertainties on amplitude and fast direction are indicated by the crosses.

and all combinations of a)–d). The variations in the retrieved values of $V_{aver}(T)$, $A^*(T)$ and θ_0 were insignificant for $V_{aver}(T)$ and $A^*(T)$, and up to 10° for θ_0. At frequencies where $A^*(T)$ was high, the difference between different estimates of θ_0 was less than 5°.

2.3.3. Observed azimuthal anisotropy

Fig. 6 shows the comparison of the bootstrap procedure with the results from the azimuth smoothing. The agreement between the two is good, in particular concerning the value of A^*.

A^* increases from approximately 0 at short periods to approximately 0.015 at 100 s period, i.e. a 3% peak to peak apparent anisotropy. The increase in A^* with period is not surprising as the crust is likely to have no large-scale azimuthal anisotropy. The increase in A^* does however only start at relatively long periods, and we shall see in Section 4 that this implies that the azimuthal anisotropy must be located well below Moho. At long periods the slope of A^* is somewhat higher in the case of azimuth smoothing than in the case of the bootstrap estimate. To use a conservative estimate of the increase of A^* with period we used the output of the bootstrap analysis for subsequent inversions.

The fast velocity direction needs to be interpreted with some caution. The scatter is relatively large and variations occur rapidly between neighbouring periods. Some of these oscillations are due to poor constraints on θ_0 when A^* is small. Considering that surface waves integrate information over a whole depth range, the oscillations are not realistic. Our conclusion on θ_0 is therefore that variations with period cannot be resolved, and that the fast direction is consistently N0–N40 at periods with significant azimuthal variation of the phase velocity.

3. Inversion

Several strategies can be followed in the inversion of surface-wave dispersion. A classical approach for phase velocity inversion is through linearised inversion. The average Rayleigh wave phase velocities have already been inverted for this region [36]. This model explains the isotropic part of the Rayleigh wave dispersion, therefore the anisotropic inversion should yield a model which does not deviate strongly from this initial model. It is consequently possible to use a linearised inversion. We used a generalised inverse procedure in which it is possible to explicitly define a priori information on both the input data and on the model. [53].

The phase velocities of Love and Rayleigh waves propagating in a flat general anisotropic structure depend on 13 of the 21 elastic coefficients of the structure. Using the notation of Montagner and Nataf [54], first-order perturbations in the phase velocity of Love waves have the following dependence on elastic coefficients:

$$\delta V_L = \frac{\partial V_L}{\partial L}(\delta L - G_C\cos 2\theta - G_S\sin 2\theta) + \frac{\partial V_L}{\partial N}(\delta N - C_C\cos 4\theta - C_S\sin 4\theta) \quad (4)$$

Similarly for Rayleigh waves, we have:

$$\delta V_R = \frac{\partial V_R}{\partial A}(\delta A + B_C\cos 2\theta + B_S\sin 2\theta + C_C\cos 4\theta + C_S\sin 4\theta) + \frac{\partial V_R}{\partial C}\delta C + \frac{\partial V_R}{\partial F}(\delta F + H_C\cos 2\theta + H_S\sin 2\theta) + \frac{\partial V_R}{\partial L}(\delta L + G_C\cos 2\theta + G_S\sin 2\theta) \quad (5)$$

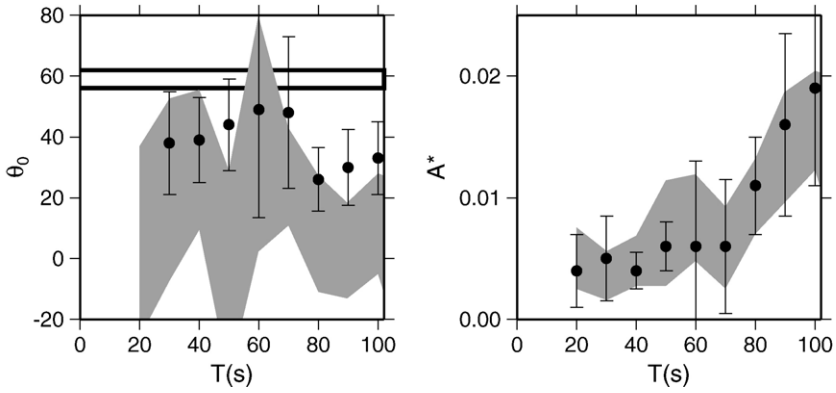

Fig. 6. Estimates of θ_0 (left) and A^* (right) using either the bootstrap procedure of Section 2.3.1 (grey shading) or through the back azimuth smoothing of Section 2.3.2 (filled circles with error bars). The peak to peak anisotropy is twice the value of A^*. The two bold lines in the left plot show the minimum and maximum azimuth of present-day absolute plate motion in the center of the array using different plate motion models (NUVEL1A, HS3-NUVEL3A,GRSM1.2,..) as calculated by the UNAVCO Facility.

Each combination of elastic coefficients contains a radial anisotropic term (A, C, F, L or N) and, in all cases but one, some azimuthal terms. The elastic coefficients related to the azimuthal terms can be separated into terms related to the cosines (with index C) and terms related to the sines (with index S). Their relation to the components of the elastic tensor is given by Montagner and Nataf [54].

Only four of the elements relating to Eqs. (4) and (5) were retrieved in the data analysis: the azimuthally averaged Love $V_{L0}(T)$ and Rayleigh $V_{R0}(T)$ wave phase velocities, the amplitude $A^*(T)$ of relative variation of Rayleigh phase velocity in 2θ, and the direction θ_0 of maximum velocity. As the direction (N0–N40) of maximum phase velocity does not vary significantly with period, we choose a coordinate system with one axis aligned along this direction. Using this coordinate system the sine terms become zero and Eqs. (4) and (5) can be used to determine the dependence of the averaged velocities and azimuthal variation on the elastic parameters. For the perturbation in Love wave average phase velocity δV_{L0} we get:

$$\delta V_{L0} = \frac{\partial V_L}{\partial L}\delta L + \frac{\partial V_L}{\partial N}\delta N. \tag{6}$$

For the perturbation in Rayleigh wave average phase velocity δV_{R0} and its azimuthal variation we get:

$$\delta V_{R0} = \frac{\partial V_R}{\partial A}\delta A + \frac{\partial V_R}{\partial C}\delta C + \frac{\partial V_R}{\partial F}\delta F + \frac{\partial V_R}{\partial L}\delta L \tag{7}$$

$$A^* = \frac{1}{V_{R0}}\left(\frac{\partial V_R}{\partial A}B_C + \frac{\partial V_R}{\partial F}H_C + \frac{\partial V_R}{\partial L}G_C\right) \tag{8}$$

where A^* is the relative amplitude of the azimuthal variation defined in Eq. (3).

Eqs. (6) and (7) are two coupled equations in the radial anisotropic elastic coefficients A, C, F, L, and N, whereas Eq. (8) is an independent equation in the parameters B_C, H_C, and G_C, which control the variation in 2θ of the structure.

We can perform two separate sets of inversions: an inversion of the averaged phase velocities of the Love and Rayleigh waves to retrieve the radial anisotropy of the structure, and an independent inversion of the azimuthal variation.

In both inversions, it is clear that we cannot resolve all the elastic parameters involved. There are two ways to solve this underdetermined problem: invert for the best resolved parameters only, or couple the parameters using a-priori information. We did both.

In inverting for the best resolved parameters, we made assumptions similar to the one made in isotropic media, which is that the phase velocity of surface waves is mostly dependent on the depth distribution of S-wave velocities and not on the variations in P-wave velocity and density. In the radial anisotropic case, this translates into the Rayleigh wave average phase velocities being mostly dependent on the depth distribution of the SV-wave velocity, or parameter L, and the Love wave average phase velocities being mostly dependent on the SH-waves velocity, or parameter N [52,54]. The azimuthal variation of the Rayleigh wave phase velocity depends mainly on the azimuthal variation of the SV-wave velocity at depth, or parameter G_C [55]. The dominance of these parameters is a consequence of the partial derivatives $\frac{\partial V_R}{\partial L}$ and $\frac{\partial V_L}{\partial N}$ being larger than the other partial derivatives in the Eqs. (6)–(8) above.

Instead of inverting for the elastic parameters L, N and G_C, we chose to use another parameterization: the SV-wave velocity, and two non-dimensional parameters ξ (degree of radial anisotropy) and $\hat{G}_C$ (degree of azimuthal anisotropy), where

$$\xi = \frac{N}{L} \tag{9}$$

and

$$\hat{G}_C = \frac{G_C}{L}. \tag{10}$$

An alternative to inverting for the best resolved parameters is to couple all the elastic coefficients involved using a-priori information. In the upper mantle, we can assume that anisotropy is dominantly related to the orientation of olivine crystals and invert for the percentage (by volume) of oriented olivine crystals in the rock, assuming that no other minerals contribute to the anisotropy. With such an inversion, it is easier to compare directly and quantitatively the results of the inversion of the Love and Rayleigh average velocities with those of the inversion of the azimuthal variation of the Rayleigh wave phase velocities. Such an inversion is possible because we can calculate the partial derivatives of the phase velocity with respect to percentage aligned olivine (see Eq. (18)).

To explain the high Love wave phase velocities observed in the present study, the fast a-axis of the olivine crystals must be dominantly horizontal [52]. Using the elastic coefficients for pure olivine crystals given by Abramson et al. [13], setting the a-axis horizontally in the reference azimuth, and supposing that the b- and

c-axes orient randomly in the perpendicular plane, we obtained the following normalised elastic coefficients for a model made of pure oriented olivine:

$$\xi_0 = 1.22 \tag{11}$$

$$\hat{G}_{C0} = 0.078 \tag{12}$$

The other anisotropic parameters are:

$$\phi_0 = C/A = 0.83 \tag{13}$$

$$\eta_0 = F/(A-2L) = 0.67 \tag{14}$$

$$\hat{B}_{C0} = B_C/A = 0.21 \tag{15}$$

$$\hat{H}_{C0} = H_C/F = -0.042 \tag{16}$$

ξ_0, ϕ_0 and η_0 parameterize the radial anisotropic component, whereas $\hat{G}_{C0}$, $\hat{B}_{C0}$ and $\hat{H}_{C0}$ are related to the azimuthal variation in 2θ.

Note that for a model of pure oriented olivine minerals with the a-axis randomly oriented in the horizontal plane instead of in a single direction, the values of ξ_0, ϕ_0 and η_0 are equal to those of the model above, but that the values of $\hat{G}_{C0}$, $\hat{B}_{C0}$ and $\hat{H}_{C0}$ are zero. The values of ξ_0, ϕ_0 and η_0 can therefore be considered as measuring the degree of alignment of the a-axis in the horizontal plane, whatever the azimuthal direction, and the values of $\hat{G}_{C0}$, $\hat{B}_{C0}$ and $\hat{H}_{C0}$ the degree of alignment of the a-axis in a given azimuthal direction.

Using the values above (Eqs. (11)–(16)) to couple the variations of the different parameters, we invert our data with respect to two proportions of oriented olivine using the following partial derivatives:

$$\frac{\partial V}{\partial p_0} = (\xi_0-1)\frac{\partial V}{\partial \xi} + (\phi_0-1)\frac{\partial V}{\partial \phi} + (\eta_0-1)\frac{\partial V}{\partial \eta} \tag{17}$$

where V is V_R or V_L, and

$$\frac{\partial A^*}{\partial p_1} = \hat{G}_{C0}\frac{\partial V_R}{\partial \hat{G}_C} + \hat{B}_{C0}\frac{\partial V_R}{\partial \hat{G}_C} + \hat{H}_{C0}\frac{\partial V_R}{\partial \hat{H}_C} \tag{18}$$

p_0, which derives from the simultaneous inversion of the Love and Rayleigh wave azimuthally averaged velocities, is the proportion of olivine crystals oriented in the horizontal plane, irrespective of the azimuth in which they are oriented. p_1, which derives from the inversion of the azimuthal variation of the Rayleigh wave phase velocities, is the proportion of olivine crystals oriented in the direction of maximum phase velocity. At depths where they have the same resolution, p_0 will be equal to p_1 in regions where all the olivine crystals are oriented in a single horizontal direction, whereas p_1 will be much smaller than p_0 in regions with random orientation of the a-axis in the horizontal plane.

Note that $\hat{B}_{C0}$ is larger than $\hat{G}_{C0}$ by a factor of four and although it is associated with a smaller partial derivative (the same as the one associated with P-waves), it may have a non-negligible influence on the azimuthal variation of the Rayleigh wave phase velocity variations due to its high amplitude in olivine crystals.

The phase velocity data were inverted in terms of elastic coefficients as a function of depth using the method of Tarantola and Valette [53]. Initial phase velocities and their partial derivatives were calculated using a program from Saito [56] in an initial model based on the inversion of the averaged Rayleigh wave phase velocities alone [36].

In the inversion [53] the smoothness of the model variations with depth can be controlled explicitly by assuming some a-priori correlation between the variations of a parameter at different depths. This control was done by building a non-diagonal a-priori model covariance matrix. The inversion is then dependent on this a-priori information and not on the discretisation with depth of the model. We used Gaussian functions as a-priori correlation functions, as in Lévêque et al. [55]. The correlation was suppressed between depth points in different layers, for example between points in the crust and in the mantle.

We explored the non-unicity of the inversion results by using three different layerings in the upper mantle: a model with continuous variations only (Model 1), and two models with two decorrelated layers, representing the lithosphere and asthenosphere. We used two different depths for the lithosphere–asthenosphere boundary, 210 km (Model 2a) and 250 km (Model 2b). The choice of depth was based on xenolith analysis [38,66] who estimated the lithospheric thickness to approximately 225–250 km. This estimate is in agreement with surface-wave models [36]. These three models do not cover all possibilities, but are sufficient to give good insight into the trade-offs of the resulting solutions.

The limited depth resolution of the fundamental-mode surface waves means that we must use relatively large correlation lengths, which in turn governs the smoothness of the model. The correlation length was set to 100 km for Model 1. In Models 2a and 2b, the correlation length was set to 400. The strong smoothing compensates for the increase in number of parameters due to the decorrelation of the

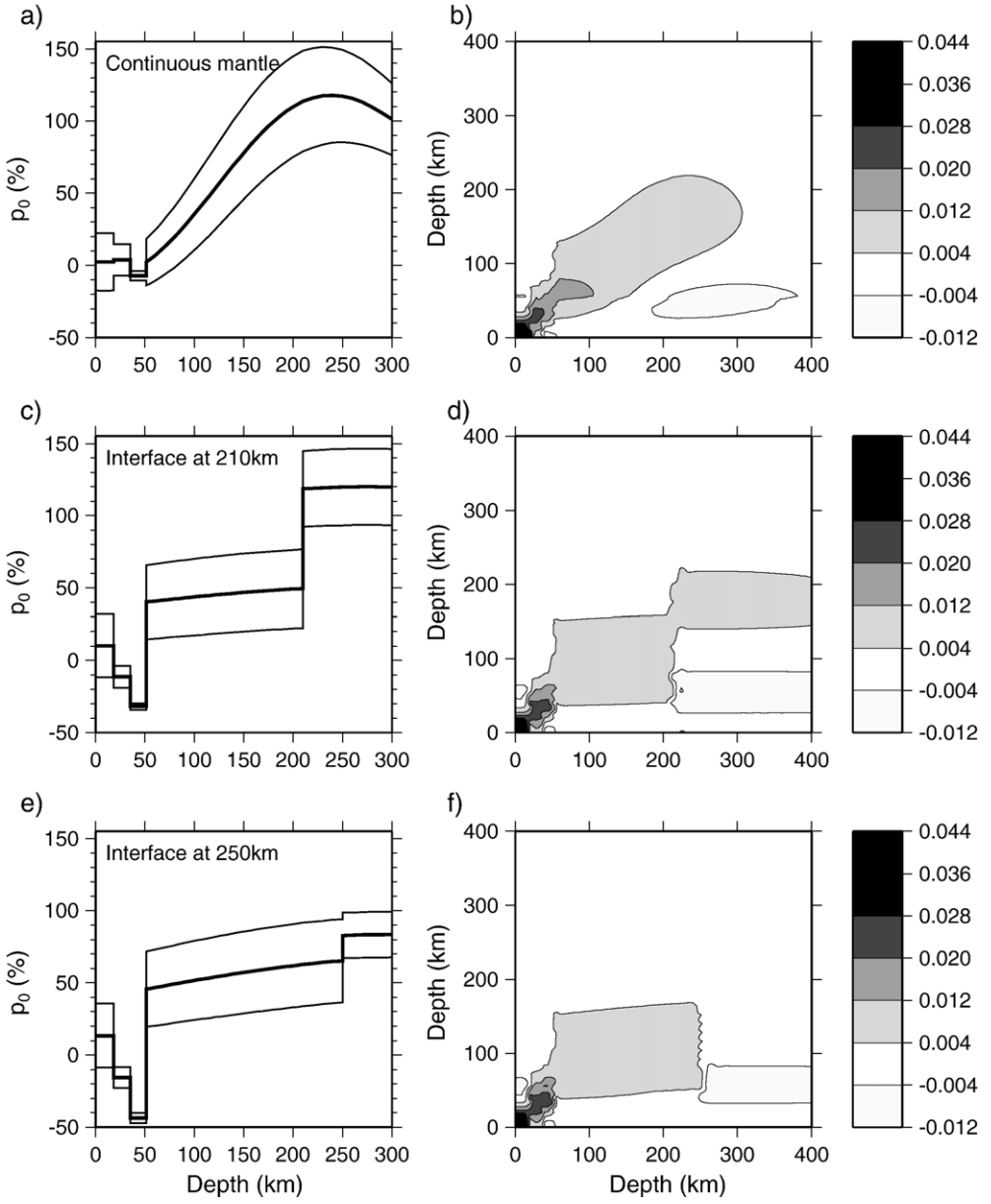

Fig. 7. Models of p_0 volume percentage olivine aligned in the horizontal plane as compared to the whole rock. The left column shows the models (a: Model 1, c: Model 2a, e: Model2b). The approximate conversion between p_0 and ξ is $\xi = 1 + 0.22 * p_0$. The thick line corresponds to the inversion of the average Love and Rayleigh dispersion values and the two thin lines to inversions where the data uncertainty has been added (subtracted) to the average dispersion in the two combinations that correspond to minimizing and maximizing the anisotropy. The plots to the right show the resolution matrices (b: Model 1, d: Model 2a, f: Model2b). Due to the application of a priori correlation lengths, the resolution is smeared over a relatively wide depth interval. In this inversion, resolution is poor below 200 km depth.

two mantle layers. The crust is approximately 51 km thick and composed of three decorrelated layers.

To present a range of acceptable models which is easy to interpret, we do not show the a posteriori model uncertainty, rather we show the results of three inversions: an inversion of the data points that corresponds to the average observation and two inversions of the data points that maximize and minimize the amount of anisotropy using data points plus (minus) their associated uncertainty. The models resulting from the two last inversions show the range of smooth models allowed by the data, under the assumption that their errors are not random, but are positive or negative biases in the average measurements.

4. Results

Fig. 7 shows the results of the inversions of Rayleigh and Love wave dispersion and Fig. 8 those for the azimuthal anisotropy. We do not show the V_{SV} model which is almost identical to that presented by Bruneton et al. [36].

As discussed in the previous section, a parameterization in terms of an equivalent rock where all anisotropy is due to aligned olivine minerals makes it possible to directly compare the two inversions. The inversion in terms of anisotropic parameters ξ and $\hat{G}_C$ produced models almost linearly related to the models in volume percentage olivine. The depth distribution of the

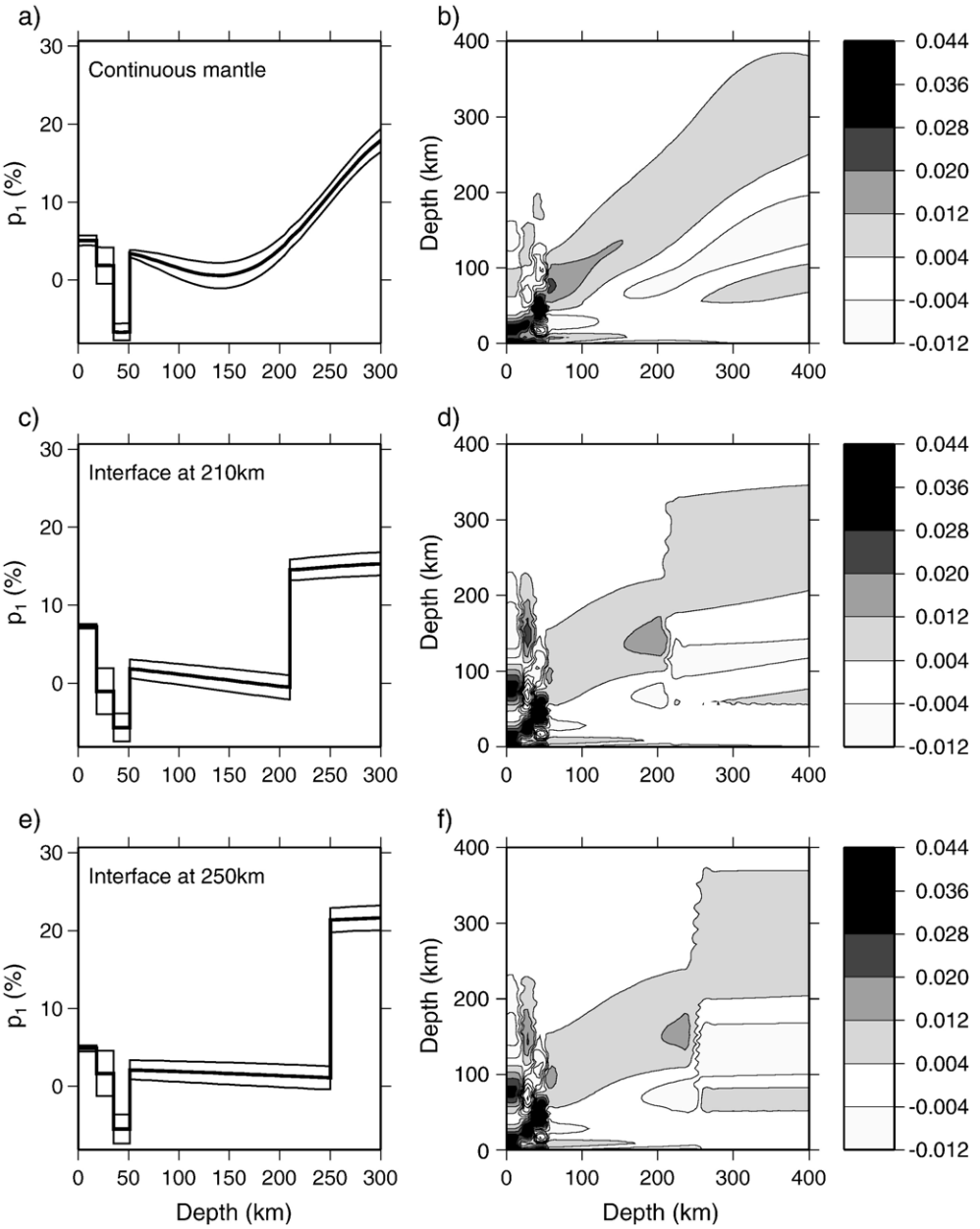

Fig. 8. Models of p_1 volume percentage olivine aligned in the fast Rayleigh wave direction as compared to the whole rock. The organisation of the figure is as in Fig. 7. Resolution is good throughout the whole depth range of the model (0–300 km). The conversion factor between p_1 and $\hat{G}_C$ is approximately 0.25.

anisotropy is similar whether we invert for elastic parameters or percentage olivine.

The conversion relation between the models in ξ and in p_0 is $\xi = 1 + 0.22 * p_0$, which corresponds exactly to the conversion implied by Eq. (11). This shows that the parameters ϕ and η, which are taken into account in the inversion with respect to the proportion of olivine crystals, play a minor role in the inversion of the Love and Rayleigh average velocities.

The conversion ratio between the models in $\hat{G}_C$ and in p_1 is $\hat{G}_C = 0.25 * p_1$. This is different from the factor of 0.078 implied by Eq. (12). This discrepancy is due to olivine crystals having large $\hat{B}_C$ values, and therefore absorbing part of the azimuthal variation when the inversion is made with respect to the proportion of olivine crystals.

Fig. 9 shows the data fit in the case of the continuous mantle model using our estimated best data points and their upper and lower limits. The two layered models give an equally good data fit.

4.1. Radial anisotropy

As shown in Fig. 7, the radial anisotropy is not resolved beneath 200 km depth, mostly due to the limited depth penetration of the fundamental-mode Love waves. The resolution is however sufficiently good within the lithosphere to indicate significant radial anisotropy, even though the variation with depth is not resolved. This can be seen by the difference between the three models with different parameterization of the mantle layers.

Model 1 shows a strong increase in p_0 with depth within the lithosphere, from 0% below Moho to 100% at 200 km depth. The latter value is unrealistic, but the inversion shows that there is some tendency for p_0 to increase with depth. The model with the lithosphere–asthenosphere boundary at 210 km depth also has very large values of p_0 at depth. Using a depth boundary at 250 km depth shows that the data can also be fully explained by a model with slowly increasing p_0 from 40% to 65% in the lithosphere. This corresponds to values ξ of approximately 1.1 to 1.14.

Due to the differences in results between different model parameterizations we cannot draw any firm conclusions on the evolution of p_0 with depth, particularly below the lithosphere. It is however clear that p_0 in the lithosphere is significant, of the order of 50%. This means that the lithosphere beneath the array is characterized by strong radial anisotropy. Olivine minerals are likely to constitute 50–80% of the mantle material in the area [38]. The values of p_0 that we obtain indicate that if the anisotropy is mainly due to olivine then almost all of these minerals must be aligned in the horizontal plane.

4.2. Azimuthal anisotropy

Fig. 8 shows the result of the inversion for azimuthal anisotropy. The resolution of the model parameters is good over the whole depth range of the model (0–300 km). The depth penetration of the fundamental-mode Rayleigh wave is larger than that of the fundamental-mode Love wave. The azimuthal anisotropy is therefore better resolved than the radial anisotropic part although we have measured the azimuthal variation of the Rayleigh wave phase velocities in the same period interval as the average Love average velocities. The depth resolution is

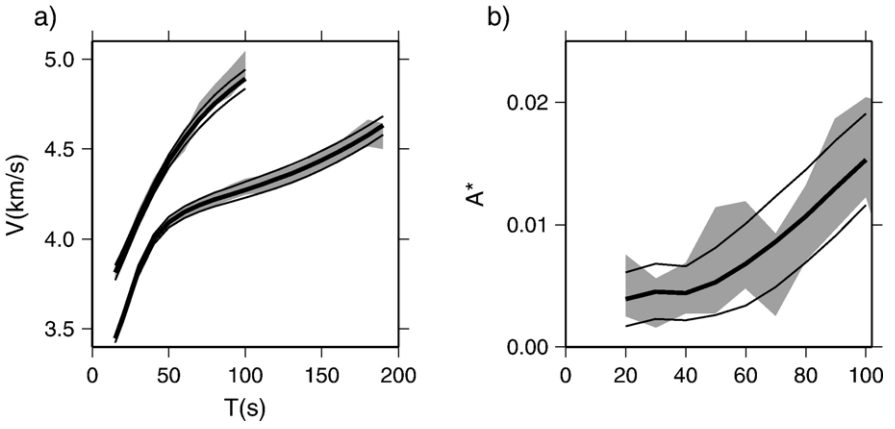

Fig. 9. Fit between observed dispersion values (grey shade) and the ones in the final inverted models. The thick lines correspond to the inversion of the average dispersion values (thick lines in Figs. 7 and 8) and the thin lines to the fit using the minimum and maximum anisotropy models (thin lines of Figs. 7 and 8). a) Rayleigh and Love dispersion. b) Apparent azimuthal anisotropy A^* of Rayleigh waves. The peak to peak anisotropy is twice the value of A^*.

however only sufficiently good to constrain the variations with depth in the top 200 km, where the models are similar in spite of different parameterizations. Below that depth the anisotropy must be significant but the depth resolution is not sufficient to well constrain the variation with depth.

In model 1, the anisotropy is negligible down to 200 km depth, from where it increases to 20% aligned olivine at 300 km depth. In Models 2a and 2b, the anisotropy is also insignificant in the lithosphere, independently of whether the decorrelation of the two layers is at 210 or 250 km depth. The amount of sub-lithospheric anisotropy corresponds to approximately 15–20% of the rock being olivine minerals aligned in the fast direction (N-NE).

The small amount of lithospheric azimuthal anisotropy does not necessarily mean that the lithospheric mantle is locally isotropic, as this may also be caused by a complex anisotropic structure for which the average azimuthal anisotropy over the array is small. This is in qualitative agreement with P-wave residual spheres at the SVEKALAPKO array: Plomerovà et al. [39] find a dominant NNE fast direction in the Archean, while the rest of the stations show complex anisotropy patterns interpreted as a complex Proterozoic–Archean boundary.

5. Discussion and conclusions

The mantle lithosphere beneath Finland has significantly different V_{SV} and V_{SH} velocities. Our estimates show that this anisotropy can be explained by 50% (volume) or more of the total rock being composed of horizontally aligned olivine minerals. Xenoliths from the area have amounts of olivine varying between 50% and 80% [38]. The majority of the olivine minerals must therefore be aligned in or close to the horizontal plane if they are the cause of the observed anisotropy.

The inversions for the ratio of elastic constants $\xi = N/L$ rather than the percentage of horizontally aligned olivine gave virtually the same model, with a simple conversion between the two parameters (see caption to Fig. 7). We obtained a ξ of approximately 1.1 to 1.14 in the lithosphere which is similar to values obtained further east in the East European Platform [57]. These values for ξ are higher than those in PREM [58] (1–1.1 in the top of the mantle) but direct comparisons are difficult as cratons only contribute modestly to average global models.

Global and large-scale 3-D models [22,25,59,60] show that there is considerable lateral variation in radial anisotropy. Overall, there seems to be some indication of smaller values of ξ beneath cratons as compared to PREM in the top part of the lithosphere and higher values between 100 and 220 km depth [59]. The absolute value of ξ over all cratons in the model of Beghein and Trampert [59] is almost constant at 1.06 over the top 220 km, i.e. almost half the amount of anisotropy found beneath Finland. Matzel and Grand [57] suggest that the radial anisotropy in the East European Platform is very small below the lithosphere, but we do not have sufficient depth resolution to resolve this in our study area.

Similar to observations from North America [26], but in contrast to observations from Australia [24,26,27], we do not find any important lithospheric azimuthal anisotropy under the SVEKALAPKO array. This may either be due to absence of preferred azimuthal olivine orientation within the horizontal plane, or to different orientations in sub-regions within the array, cancelling the overall effect on the surface-wave phase velocities. The second explanation is the most likely one in our case, as P-wave residuals observed on the SVEKALAPKO stations [39] show that the anisotropy in the area is complex and separated into at least three different domains.

Our data do therefore not exclude the presence of significant amounts of azimuthal anisotropy in the lithosphere, which seems to dominate azimuthal anisotropy on a global scale [24].

We observe significant azimuthal anisotropy below 200–250 km depth, which can be explained by approximately 15–20% of the rock being olivine with the a-axis aligned horizontally towards N0–N40. This fast direction is the same as observed in P-wave residuals in the Archean domain [39] and in preliminary results of SKS measurements [40]. The direction of anisotropy at sub-lithospheric depths is also in good agreement with the fast directions in the area of a recent global study [24] and a more regional study [61].

N0–N40 is significantly different from the present absolute plate motion (N55–N62, as calculated by the UNAVCO Facility's Plate Motion Calculator). The absolute N–S velocity of Baltica is presently estimated to be approximately 15 mm per year [67], corresponding well to the north–south projection of the absolute plate motion, estimated at 21–22 mm/year in the direction N60. Interestingly, the history of N–S movement does not show any trace of major changes over the last 100 Ma (Torsvik et al., in preparation). We do therefore not have any indication of major changes in flow directions beneath Baltica over this time period. Using the formulation of Kaminski [62], the timescales involved are much longer than what is necessary for the alignment of olivine in the case of simple shear.

There could be at least three explanations for the discrepancy between the observed fast direction and the absolute plate motion. Firstly, that there is some degree

of anisotropy for which the fast direction corresponds to an older flow direction up to approximately 300 km depth. This would however be in strong disagreement with both xenolith and surface-wave derived lithospheric thickness in the area [36,38,66]. Secondly, that rapid lateral changes of the anisotropy may induce systematic errors in the estimate of the average anisotropy. The overall agreement between the fast directions obtained by surface wave and preliminary body wave analysis would at the present stage not support this explanation. Finally, that the flow pattern beneath Finland may be more complex than predicted from simple flow parallel to plate motion. Complex sublithospheric flow patterns have for example been invoked to explain SKS splitting in North America [63,64].

The deep azimuthal anisotropy that we observe is significantly higher than that observed by surface wave analysis on a global scale and for the North Atlantic area [24,61]. These studies have a better depth resolution than ours due to the use of higher modes. Pilidou et al. however [61] show on synthetic data that their lateral resolution is significantly poorer for azimuthal anisotropy than for isotropic velocity variations and that the anisotropy that they estimate is overall significantly smaller (in particular in our study area) than the one of their input test model even though the recovered directions generally are correct.

The presence of moderate, deep azimuthal anisotropy beneath Finland, combined with the difference in fast direction to that predicted from absolute plate motion, strongly suggests that flow beneath continents is complex and that shields are not coupled to the convecting mantle in a simple way.

Acknowledgements

H.A. Pedersen gratefully acknowledges the Alexander von Humboldt Foundation for financing research at the GeoForschungsZentrum Potsdam and the University of Potsdam, Germany. M. Bruneton acknowledges C.J. Thomson for financing her research through his NSERC discovery grant at Queen's University, Kingston, Canada.

We thank H.J. Reichmann for discussions on appropriate references on the elastic parameters of olivine and Trond Torsvik for new information on the absolute plate motion of Baltica over the last 500 Ma. J. Plomerová kindly provided us with information of body-wave anisotropy beneath the SVEKALAPKO array, and we thank her for fruitful discussions over the years of the SVEKALAPKO project. E. Kaminski clarified how to calculate the time necessary for alignment of olivine minerals in the context of the Baltic Shield. The absolute plate motions were calculated by the UNAVCO Facility. Figures were created with the GMT software [65]. We thank two anonymous reviewers for thoughtful and constructive reviews.

The following institutions participate in the SVEKALAPKO project: the Universities of Oulu, Helsinki, Uppsala, Grenoble, Strasbourg, Stuttgart, St. Petersburg, the Kola Science Center, The Institute of Physics of the Earth Moscow, ETH Zurich, GFZ Potsdam, The Geophysical Institute of CAS Prague, and Spezgeofisika MNR Moscow. The SVEKALAPKO project has been supported by national science funding agencies in Finland, France, Sweden and Switzerland, by the Institute of Geophysics of the Polish Academy of Sciences, by GeoForschungsZentrum Potsdam (GFZ), by the GFZ Geophysical Instrument Pool, by the Réseau Large Bande Mobile (France), and by an EU INTAS grant. The European Science Foundation provided funding for several SVEKALAPKO Workshops within the framework of EUROPROBE.

The SVEKALAPKO Seismic Tomography Group is formed by: U. Achauer, A. Alinaghi, J. Ansorge, G. Bock, M. Bruneton, W. Friederich, M. Grad, A. Guterch, P. Heikkinen, S.E. Hjelt, T. Hyvonen, J.P. Ikonen, E. Kissling, K. Komminaho, A. Korja, E. Kozlovskaya, M. V. Nevsky, H. Paulssen, N. Pavlenkova, H.A. Pedersen, J. Plomerov´a, T. Raita, O. Riznitchenko, R.G. Roberts, S. Sandoval, I.A. Sanina, N. Sharov, Z.H. Shomali, J. Tiikkainen, E. Wielandt, K. Wylegalla, J. Yliniemi and Y.G. Yurov.

References

[1] T.H. Jordan, The continental tectosphere, Rev. Geophys. 13 (1975) 1–12.

[2] S. Sandoval, E. Kissling, J. Ansorge, The SVEKALAPKO STWG, High-resolution body wave tomography beneath the SVEKALAPKO array: II. Anomalous upper mantle structure beneath central Baltic Shield, Geophys. J. Int. 157 (2004) 200–214.

[3] D.E. James, M.J. Fouch, J.C. VanDecar, S. van der Lee, The Kaapvaal Seismic Group, Tectospheric structure beneath southern Africa, Geophys. Res. Lett. 28 (2001) 2485–2488.

[4] E. Debayle, B.L.N. Kennett, K. Priestley, The Australian continental upper mantle: structure and deformation inferred from surface waves, J. Geophys. Res. 105 (2000) 25423–25450.

[5] K. Priestley, E. Debayle, Seismic evidence for a moderately thick lithosphere beneath the Siberian Platform, Geophys. Res. Lett. 30 (2003), doi:10.1029/2002GL015931.

[6] A. Nicolas, N.I. Christensen, Formation of anisotropy in upper mantle peridotites: a review, in: K. Fuchs, C. Froidevaux (Eds.), Composition, structure and dynamics of the lithosphere–asthenosphere system, Geodyn. Ser., vol. 16, AGU, Washington D.C., 1987, pp. 111–123.

[7] T.W. Becker, J.B. Kellogg, G. Ekström, R.J. O'Connell, Comparison of azimuthal seismic anisotropy from surface waves and finite strain from global mantle-circulation models, Geophys. J. Int. 155 (2003) 696–714.
[8] C. Gaboret, A.M. Forte, J.-P. Montagner, The unique dynamics of the Pacific Hemisphere mantle and its signature on seismic anisotropy, Earth Planet. Sci. Lett. 208 (2003) 219–233.
[9] S. Zhang, S.-I. Karato, Lattice preferred orientation of olivine aggregates deformed in simple shear, Nature 375 (1995) 774–777, doi:10.1038/375774a0.
[10] E. Kaminski, N.M. Ribe, Timescales for the evolution of seismic anisotropy in mantle flow, G3, 3 (2002), doi:10.1029/2001GC000222.
[11] D.G. Issak, High-temperature elasticity of iron-bearing olivine, J. Geophys. Res. 97 (1992) 1871–1885.
[12] S.L. Webb, The elasticity of the upper mantle orthosilicates olivine and garnet to 3 GPa, Phys. Chem. Miner. 16 (1989) 684–692.
[13] E.H. Abramson, J.M. Brown, L.J. Slutsky, J. Zaug, The elastic constants of San Carlos olivine to 17 GPa, J. Geophys. Res. 102 (1997) 12253–12263.
[14] P. Silver, D. Mainprice, W. Ben Ismail, A. Tommasi, G. Barruol, Mantle structural geology from seismic anisotropy, in: Y. Fei, C.M. Bertka, B.O. Mysen (Eds.), Mantle petrology: field observations and high pressure experimentations: a tribute to Francis R. Boyd, The Geochemical Society Special publication, vol. 6, 1999, pp. 79–103.
[15] H. Jung, S.I. Karato, Water-induced fabric transitions in olivine, Science 293 (2001) 1460–1463.
[16] R.F. Cooper, D.L. Kohlstedt, Rheology and structure of olivine–basalt partial melts, J. Geophys. Res. 91 (1986) 9315–9323.
[17] K.B. Holtzman, D.L. Kohlstedt, M.E. Zimmerman, F. Heidelbach, T. Hiraga, J. Hustoft, Melt segregation and strain partitioning: implications for seismic anisotropy and mantle flow, Science 301 (2003) 1227–1230.
[18] S. Crampin, A review of wave motion in anisotropic and cracked elastic media, Wave Motion 3 (1981) 343–391.
[19] M.K. Savage, Seismic anisotropy and mantle deformation: what have we learned from shear wave splitting? Rev. Geophys. 37 (1999) 65–106.
[20] N.I. Christensen, M.H. Salisbury, Seismic anisotropy in the oceanic upper mantle: evidence from the Bay of Islands ophiolite complex, J. Geophys. Res. 84 (1979) 4601–4610.
[21] M. Toriumi, Preferred orientation of olivine in mantle-derived peridotites and stress in the lithosphere, J. Phys. Earth 32 (1984) 259–271.
[22] J.-P. Montagner, T. Tanimoto, Global upper mantle tomography of seismic velocities and anisotropies, Geophys. J. Res. 96 (1991) 20337–20351.
[23] G. Ekström, A.M. Dziewonski, The unique anisotropy of the Pacific upper mantle, Nature 394 (1998) 168–172.
[24] E. Debayle, B.L.N. Kennett, K. Priestley, Global azimuthal seismic anisotropy and the unique plate-motion deformation of Australia, Nature 433 (2005) 509–512.
[25] Y. Gung, M. Panning, B. Romanowicz, Global anisotropy and the thickness of continents, Nature 422 (2003) 707–711.
[26] A. Li, D.W. Forsyth, K.M. Fischer, Shear velocity structure and azimuthal anisotropy beneath eastern North America from Rayleigh wave inversion, J. Geophys. Res. 108 (2003), 2362 doi:10.1029/2002JB002259.
[27] F.J. Simons, R.D. van der Hilst, Seismic and mechanical anisotropy and the past and present deformation of the Australian lithosphere, Earth Planet. Sci. Lett. 211 (2003) 271–286.
[28] J.-P. Montagner, D.-A. Griot-Pommera, J. Lavé, How to relate body wave and surface wave anisotropy? J. Geophys. Res. 105 (2000) 19015–19027.
[29] L.P. Vinnik, R.W.E. Green, L.O. Nicolaysen, Recent deformations of the deep continental roots in southern Africa, Nature 375 (1995) 50–52.
[30] M. Freybourger, J.B. Gaherty, T.H. Jordan, The Kaapvaal Seismic Group, Structure of the Kaapvaal craton from surface waves, Geophys. Res. Lett. 28 (2001) 2489–2492.
[31] R.L. Saltzer, Upper mantle structure of the Kaapvaal craton from surface wave analysis—a second look, Geophys. Res. Lett. 29 (2002) 1093, doi:10.1029/2001GL013702.
[32] E. Debayle, B.L.N. Kennett, Anisotropy in the Australian upper mantle from Love and Rayleigh waveform inversion, Earth Planet. Sci. Lett. 184 (2000) 339–351.
[33] J.B. Gaherty, A surface wave analysis of seismic anisotropy beneath eastern North America, Geophys. J. Int. 158 (2004) 1053–1066.
[34] G. Bock, The SVEKALAPKO Seismic Tomography Working Group (SSTWG), Seismic probing of the fennoscandian lithosphere, EOS Trans. AGU 82 (621) (2001) 628–629.
[35] A. Alinaghi, G. Bock, R. Kind, W. Hanka, K. Wylegalla, TOR and SVEKALAPKO groups, Receiver function analysis of the crust and upper mantle from the North German Basin to the Archean Baltic Shield, Geophys. J. Int. 155 (2003) 641–652.
[36] M. Bruneton, H.A. Pedersen, P. Vacher, I.T. Kukkonen, N.T. Arndt, S. Funke, W. Friederich, V. Farra, The SVEKALAPKO Seismic Tomography Working Group, Layered lithospheric mantle in the central Baltic Shield from surface waves and xenolith analysis, Earth Planet. Sci. Lett. 226 (2004) 41–52.
[37] M. Bruneton, H.A. Pedersen, V. Farra, N.T. Arndt, P. Vacher, The SVEKALAPKO Seismic Tomography Working Group, Complex lithospheric structure under the central Baltic Shield from surface wave tomography, J. Geophys. Res. 109 (2004) B10303.
[38] I.T. Kukkonen, K. Kinnunen, P. Peltonen, Mantle xenoliths and thick lithosphere in the Fennoscandian Shield, Phys. Chem. Earth 28 (2003) 349–360.
[39] J. Plomerová, V. Babuška, L. Vecsey, E. Kozlovskaya, T. Raita, SSTWG, Proterozoic–Archean boundary in the upper mantle of eastern Fennoscandia as seen by seismic anisotropy, J. Geodyn. (in press) doi:10.1016/j.jog.2005.10.008.
[40] L. Vecsey, J. Plomerová, E. Kozlovskaya, V. Babuška, SSTWG, Shear-wave splitting as a diagnostic of varying upper mantle structure beneath south-eastern Fennoscandia, submitted for publication.
[41] E. Herrin, T. Goforth, Phase-matched filters: application to the study of Rayleigh waves, Bull. Seismol. Soc. Am. 67 (1977) 1259–1275.
[42] A.V. Lander, A.L. Levshin, Recording, identification, and measurement of surface wave parameters, in: V.I. Keilis-Borok (Ed.), Seismic Surface Waves in Laterally Inhomogeneous Earth, Kluwer Academic Publishers, Dordrecht, 1989, pp. 131–182.
[43] H.A. Pedersen, O. Coutant, A. Deshamps, M. Soulage, N. Cotte, Measuring surface wave phase velocities beneath small broadband arrays: test of an improved algorithm and application to the French Alps, Geophys. J. Int. 154 (2003) 903–912.
[44] N. Wiener, Time Series, M.I.T. Press, Cambridge, Massachusetts, 1949 (163 pp.).
[45] H.J. Hwang, B.J. Mitchell, Interstation surface wave analysis by frequency domain Wiener deconvolution and modal isolation, Bull. Seismol. Soc. Am. 76 (1986) 847–864.

[46] M.L. Smith, F.A. Dahlen, The azimuthal dependence of Love and Rayleigh wave propagation in a slightly anisotropic medium, J. Geophys. Res. 78 (1973) 3321–3333.
[47] D. Alsina, R. Snieder, V. Maupin, A test of the great circle approximation in the analysis of surface waves, Geophys. Res. Lett. 11 (1993) 633–636.
[48] N. Cotte, H.A. Pedersen, M. Campillo, V. Farra, Y. Cansi, Off-great-circle propagation of intermediate-period surface waves observed on a dense array in the French Alps, Geophys. J. Int. 142 (2000) 825–840.
[49] B.L.N. Kennett, K. Yoshizawa, A reappraisal of regional surface wave tomography, Geophys. J. Int. 150 (2002) 37–44.
[50] E. Wielandt, Propagation and structural interpretation of non-plane waves, Geophys. J. Int. 113 (1993) 45–53.
[51] W. Friederich, E. Wielandt, S. Stange, Non-plane geometries of seismic surface wavefields and their implications for regional surface-wave tomography, Geophys. J. Int. 119 (1994) 931–948.
[52] V. Maupin, Partial derivatives of surface wave phase velocities for flat anisotropic models, Geophys. J. R. Astron. Soc. 83 (1985) 379–398.
[53] A. Tarantola, B. Valette, Generalized nonlinear inverse problems solved using the least squares criterion, Rev. Geophys. Space Phys. 20 (1982) 219–232.
[54] J.-P. Montagner, H.-C. Nataf, A simple method for inverting the azimuthal anisotropy of surface waves, J. Geophys. Res. 91 (1986) 511–520.
[55] J.-J. Lévêque, M. Cara, D. Rouland, Waveform inversion of surface wave data: test of a new tool for systematic investigation of upper mantle structures, Geophys. J. Int. 104 (1991) 565–581.
[56] M. Saito, Disper 80: a subroutine package for the calculation of seismic modes solutions, in: D.J. Doornbos (Ed.), Seismological Algorithms, Academic Press, New York, 1988.
[57] E. Matzel, S.P. Grand, The anisotropic seismic structure of the East European platform, J. Geophys. Res. 109 (2004) B01302, doi:10.1029/2001JB000623.
[58] A.M. Dziewonski, D.L. Anderson, Preliminary reference Earth model, Phys. Earth Planet. Inter. 25 (1981) 25297–25356.
[59] C. Beghein, J. Trampert, Probability density functions for radial anisotropy from fundamental mode surface wave data and the Neighbourhood Algorithm, Geophys. J. Int. 157 (2004) 1163–1174, doi:10.1111/j.1365-246X.2004.022235x.
[60] V. Babuška, J.-P. Montagner, J. Plomerová, N. Girardin, Age-dependent largescale fabric of the mantle lithosphere as derived from surface-wave velocity anisotropy, Pure Appl. Geophys. 151 (1998) 257–280, doi:10.1007/s000240050114.
[61] S. Pilidou, K. Priestley, O. Gudmundsson, E. Debayle, Upper mantle S-wave speed heterogeneity and anisotropy beneath the North Atlantic from regional surface wave tomography: the Iceland and Azores plumes, Geophys. J. Int. 159 (2004) 1057–1076.
[62] E. Kaminski, The influence of water on the development of lattice preferred orientation in olivine aggregates, Geophys. Res. Lett. 29 (2002), doi:10.1029/2002GL014710.
[63] M.J. Fouch, K.M. Fischer, M.E. Wysession, T.J. Clarke, Shear wave splitting, continental keels, and patterns of mantle flow, J. Geophys. Res. 105 (2000) 6255–6276.
[64] D. Eaton, A. Frederiksen, S.-Y. Miong, Shear-wave splitting observations in the lower Great Lakes region: evidence for regional anisotropic domains and keel-modified asthenospheric flow, Geophy. Res. Lett. 31 (2004) L07610, doi:10.1029/2004GL019438.
[65] P. Wessel, W.H.F. Smith, New, improved version of generic mapping tools released, EOS Trans. AGU 79 (1998) 579.
[66] T.H. Torsvik, R.D. Müller, R. Van der Voo, B. Steinberger, C. Gaina, Global plate motion frames: toward a unified model, Earth Sci. Rev. (submitted for publication).
[67] K. Priestley, D. McKenzie, The thermal structure of the lithosphere from shear wave velocities, Earth Planet. Sci. Lett. (in press).